THE JOURNAL OF
PHYSICAL CHEMISTRY C

Article

pubs.acs.org/JPCC

Electronic Structures of Antimony Oxides

Jeremy P. Allen,*[†] John J. Carey,[†] Aron Walsh,[‡] David O. Scanlon,[§] and Graeme W. Watson*[†]

[†]School of Chemistry and CRANN, Trinity College Dublin, Dublin 2, Ireland

[‡]Centre for Sustainable Technologies and Department of Chemistry, University of Bath, Claverton Down, Bath BA2 7AY, United Kingdom

[§]Kathleen Lonsdale Materials Chemistry, Department of Chemistry, University College London 20 Gordon Street, London WC1H 0AJ, United Kingdom

ABSTRACT: This study details density functional theory calculations on all the polymorphs of the binary oxides of antimony (Sb_2O_3, Sb_2O_4, and Sb_2O_5) to assess the electronic structures and differences in bonding between Sb^{III} and Sb^V ions with oxygen. The results show that lone-pair formation is via a similar mechanism to other main group elements which exhibit an oxidation state of two less than the group valence, through direct interaction of Sb 5s and O 2p states, with the antibonding interaction stabilized by Sb 5p states. Furthermore, structural distortion of the Sb site directly affects the strength of the resulting lone pair. In addition to the analysis of the density of states and charge density, band structures and optical absorption spectra are also detailed. The results indicate that all materials are indirect band gap materials, with the exception of the *β*-polymorphs of Sb_2O_3 and Sb_2O_4. In addition, the fundamental and optical band gaps of the materials are found to decrease from Sb_2O_3 to Sb_2O_4 to Sb_2O_5. Calculated band-edge effective masses suggest that *β*-Sb_2O_3 may exhibit reasonable p-type properties. Furthermore, *β*-Sb_2O_3, *γ*-Sb_2O_3, and Sb_2O_5 possess low electron effective masses which are conducive with strong n-type conduction.

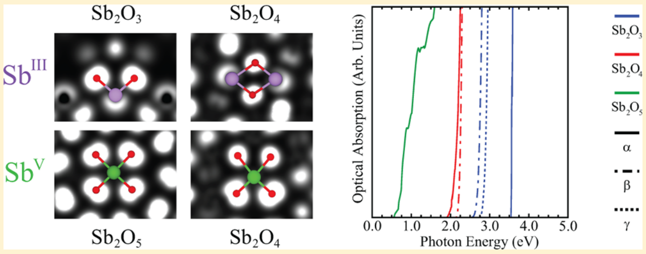

INTRODUCTION

Antimony is known to form three binary oxides, possessing either Sb^{III} (Sb_2O_3), Sb^V (Sb_2O_5), or a mixture of the two oxidation states (Sb_2O_4), with the former having the greatest commercial importance. The primary use of Sb_2O_3 is as a flame retardant, in combination with halogenated materials, for textiles, polymers, and coatings.[1−3] In addition, Sb_2O_3 has useful catalytic properties, which are mainly utilized in the production of polyethylene terephthalate.[4,5] Sb_2O_4 is also widely used as a catalyst, with other metal oxides (e.g., Fe_2O_3 and MoO_2), in the oxidation and ammoxidation of hydrocarbons.[6−11] Sb_2O_5, which is metastable at moderate temperatures,[12] is primarily used in Ru/Ir-coated Sb_2O_5-doped SnO_2 anodes for the production of hydrogen.[13,14] Antimony is also commonly used as a dopant to enhance a material's properties. For example, doping the transparent conducting oxide SnO_2 with Sb^{III} decreases the conductivity to that of an insulator, whereas doping with Sb^V enhances its n-type conductivity.[15,16] Alternatively, doping n-type ZnO with Sb^{III} has been reported to make the material a p-type conductor.[17]

Based on the group valence of V, the existence and prevalence of an oxidation state of III may be considered as unusual for antimony; however, an oxidation state of two less than the group valence is also seen for other heavy main group elements, for example, those in groups 13 (Tl^I), 14 (Pb^{II}, Sn^{II}), and 15 (Bi^{III}). Traditionally, the stability of these oxidation states is explained through the inert-pair effect.[18] Intratomic hybridization between the cation s and p states occurs forming a nonbonding sp orbital, where a lone pair of electrons can reside. Although chemically inert, as it does not take place in bonding, this inert pair is stereochemically active and, according to valence shell electron pair repulsion (VSEPR) theory, causes asymmetric coordination environments in the compounds of these species,[19,20] for example, the distorted litharge structures of SnO and PbO.[21] However, one of the failures of this approach is its inability to explain why compounds with the same cation show different levels of lone-pair activity; for example, SnTe and PbTe have perfectly symmetric rocksalt structures. This has typically been attributed to changes in the covalency of the bonds from O to Te.[20] A similar discussion has also been made for antimony chalcogenide structures.[22]

This classical model of an inert lone pair was initially challenged by Watson and Parker using density functional theory (DFT) simulations of *α*-PbO in the litharge and undistorted CsCl structures.[23,24] Their work showed that the lone pair was not formed though a chemically inert sp hybrid orbital but from an interaction of cation s and oxygen p states resulting in the formation of bonding and antibonding states. The structural distortion then allows the unoccupied cation p states to mix and stabilize these filled antibonding states, resulting in the asymmetric density. Without the anion interaction, the energy difference between the cation s and p

Received: March 15, 2013
Revised: June 18, 2013
Published: June 18, 2013

dx.doi.org/10.1021/jp4026249 | J. Phys. Chem. C 2013, 117, 14759−14769

states is too large for direct hybridization. Subsequent work on the other monochalcogenides of Sn and Pb showed that, as the anion changed from O to Te, the energy of the anion p states increased relative to the cation states.[25−28] This causes a reduction in the mixing between cation s and anion p states, and hence the lone pair is reduced due to less antibonding states for the cation p states to mix with. For SnTe and PbTe, the cation lone pair is sufficiently weakened that the increase in energy due to the reduced coordination of the distorted structures out-weighs the electronic energy gain of distortion and thus symmetric structures are observed. This model of lone-pair formation was also confirmed through X-ray emission and photoelectron spectroscopies.[29−31] Similar work has also been conducted on Bi_2O_3, with both computational and experimental studies suggesting that the Bi^{III} lone pair and structural distortion was caused by the same mechanism.[32] In addition, DFT has been utilized to investigate other lone-pair materials, examining the chemical origin of lone pairs in distorted structures, for example, $BiMnO_3$[33] and BiB_3O_6,[34] and visualizing electron densities and electron localization functions in materials containing Sn^{II}, Pb^{II}, and Bi^{III}.[35−40]

Although stable Sb^{III} compounds also exhibit structural distortions associated with asymmetric density, there has been little detailed analysis of the electronic structures or bonding in the binary Sb oxides, with most studies simply attributing any asymmetry to the formation of a nonbonding lone pair in accordance with VSEPR theory. A recent study to go beyond this view was that of Matsumoto et al.,[41] which detailed the electronic structure of As, Sb, and Bi sesquioxides. Through the modeling of a range of different structure types, their study found that formation of the lone pair played an essential role in determining the structure, stability, and properties of these materials, with the asymmetric density and structural distortion reducing from As to Sb to Bi. They also used density of states analysis to show that the presence of asymmetric density correlated with the amount of mixing between the cation p states and the antibonding cation s−O p interaction at the top of the valence band. Other studies of α-Sb_2O_3 have focused on its structural and electrical properties[42−45] and its characterization with Raman spectroscopy.[5,46−48] Similarly, the majority of the previous studies on the mixed valence oxide, Sb_2O_4, have also typically focused on the structure/Raman spectra.[47,49] Due to its use as a mixed-oxide catalyst, there has been additional study of the defect chemistry associated with dopants in Sb_2O_4. For example, Moore and Widatallah reported that the dominant intrinsic defect in the low temperature α-form is an oxygen Frenkel and that the incorporation of Fe^{III} into the structure occurs via substitution with Sb^{III} ions.[50] The doping of the β-form with V and Mo was also studied by Teller et al.[51] Sb_2O_5 has been the subject of much fewer studies, although an electronic density of states was generated by Du et al. using DFT.[52]

The aim of this study is to provide a comprehensive analysis of the three binary oxides of antimony (Sb_2O_3, Sb_2O_4, and Sb_2O_5) using DFT. Not only will this provide an understanding of the differences in atomic structure, electronic structure, and bonding of Sb^{III} and Sb^{V} atoms, but it will also allow any observed structural distortions to be rationalized. Furthermore, an understanding of the bonding in these binary oxides may assist future studies through an increased understanding of the role antimony plays in ternary materials and as a functional dopant. All polymorphs for Sb_2O_3 and Sb_2O_4 will be modeled, although focus will be primarily directed toward the most thermodynamically stable. An understanding of the electronic structure of the less-stable polymorphs is important as it enables the effect of minor impurity phases on the electrical properties to be elucidated. The features of the band structures and the band-edge effective masses of these oxides will also be assessed to examine their electrochemical properties.

■ COMPUTATIONAL METHODS

The periodic DFT code VASP[53,54] was employed for all calculations, which uses a plane-wave basis set to describe the valence electronic states. The exchange and correlation was treated with the generalized gradient approximation (GGA) via the Perdew−Burke−Ernzerhof[55] (PBE) gradient-corrected functional. Interactions between the cores (Sb:[Kr]$4d^{10}$ and O:[He]) and the valence electrons were described using the projector-augmented wave[56,57] method. Although higher levels of theory may give rise to quantitative differences for some calculated properties, GGA has been shown to be accurate at predicting lone-pair activity in other systems, such as PbO/Pbs and Sn*Ch* (*Ch* = O, S, Se, Te).[27,28]

The equilibrium lattice constants for each bulk antimony oxide were determined by optimizing the structure at a series of volumes. In each case, a constant volume constraint was applied, while allowing the atomic positions, lattice vector, and cell angles to relax. The resulting energy−volume curves were fitted to the Murnaghan equation of state to obtain the equilibrium bulk cell volume.[58] This approach minimizes potential problems of Pulay stress and changes in basis set which can accompany volume changes in plane-wave calculations. Although the Pulay stress can be anisotropic, the accuracy of this approach was confirmed previously for SnO through consideration of the pressure along different vector directions at a plane-wave cutoff of 1000 eV.[59] A plane-wave cutoff of 500 eV was found to be sufficient for all three materials, and *k*-point grids of 6 × 6 × 6, 6 × 2 × 4, 2 × 4 × 4, 8 × 6 × 4, 4 × 4 × 4, and 6 × 6 × 6 were used for α-Sb_2O_3, β-Sb_2O_3, γ-Sb_2O_3, α-Sb_2O_4, β-Sb_2O_4, and Sb_2O_5, respectively, generated using the Monkhorst−Pack scheme.[60] Primitive unit cells were used for α-Sb_2O_3, β-Sb_2O_4, and Sb_2O_5 structures. Calculations were deemed to be converged when the forces on all the atoms were less than 0.01 eV $Å^{-1}$. To determine the formation energies for each oxide, Sb metal was simulated using a Γ-centered 15 × 15 × 15 grid, and O_2 was modeled in its triplet state in a 16 $Å^3$ box with a single *k*-point at Γ. DFT is known to underbind O_2 by up to 0.7 e V,[61−63] and this is, therefore, expected to lead to an underestimation of the formation energies relative to experiment. However, as it is not possible to decouple this error from that which results from a lack of dispersion forces, the calculated energies presented here are uncorrected. To calculate the partial density of states, the wave functions were projected onto spherical harmonics centered on each atom with a radius of 1.45, 1.15, and 1.55 Å for Sb^{III}, Sb^{V}, and O, respectively. These radii were found to give reasonable space filling and electron occupations for each material.

The optical absorption spectra, as well as the optical transition matrices, were calculated within the transversal approximation.[64] This approach sums all direct valence band (VB) to conduction band (CB) transitions on the *k*-point grids to determine the optical absorption but does not include indirect and intraband transitions.[65] As only single-particle transitions are included, electron−hole correlations are not treated and would require higher-order electronic structure

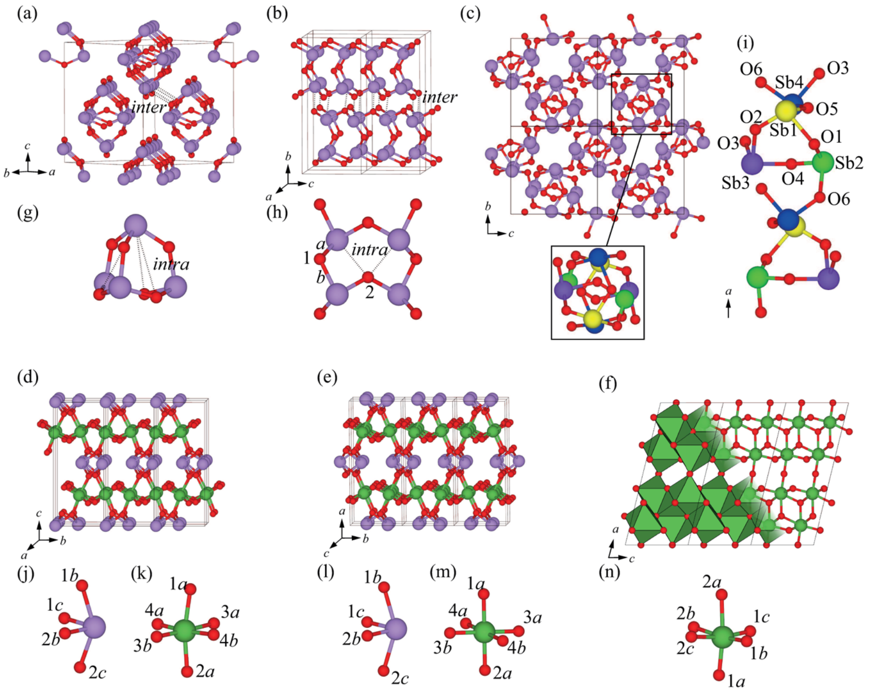

Figure 1. Structures of the (a) α-Sb_2O_3,[74] (b) β-Sb_2O_3,[74] (c) γ-Sb_2O_3,[76] (d) α-Sb_2O_4,[85] (e) β-Sb_2O_4,[85] and (f) Sb_2O_5[83,84] unit cells. Bonding environments are shown in more detail for Sb^{III} ions in (g) α-Sb_2O_3, (h) β-Sb_2O_3, (i) γ-Sb_2O_3, (j) α-Sb_2O_4, and (l) β-Sb_2O_4, and Sb^V ions in (k) α-Sb_2O_4 and (m) β-Sb_2O_4 and (n) Sb_2O_5. Sb^{III}, Sb^V, and O atoms are colored purple, green, and red, respectively. For the inset of (c) and part (i), the different Sb^{III} environments are colored purple, blue, green, and yellow for clarity.

methods.[66,67] However, this approach has been shown to provide reasonable optical absorption spectra in comparison to experiment.[68−72]

All structural figures, including those showing partial charge density, were generated using the VESTA package.[73]

■ RESULTS

Structural Prediction. The two oxidation states available to antimony give rise to three oxide stoichiometries: Sb_2O_3, Sb_2O_5, and Sb_2O_4. The first of these, Sb_2O_3, forms three different polymorphs, detailed in Figure 1a−c. The α-form, senarmontite, is the most commonly reported and most thermodynamically stable. It possess a cubic cell (space group $Fd\bar{3}m$) and comprises discrete Sb_4O_6 molecular units.[74] Within these cage structures, each O atom is bound between two Sb atoms in a bent manner, while the Sb atoms are connected to three O atoms. The O atoms form the base of a tetrahedron, with the fourth vertex, which faces away from the cluster, vacant. Under increased temperature, 843−879 K, the structure transforms to the β-valentinite phase (space group *Pccn*), containing stacked ladder-like structures in an orthorhombic habit.[74,75] These ladder-like structures form chains which run along the *c* axis of the cell and are held together by nonbonding dispersion forces. As with the α-form, the Sb and O ions are three- and two-coordinate, respectively, with similar geometries to those in the Sb_4O_6 cages. Finally, an orthorhombic γ-phase (space group $P2_12_12_1$) has been reported under high temperatures and pressures of 573−773 K and 9−11 GPa.[76] This orthorhombic structure consists of interlocking rod-like structures which result in the formation of pores along the *a* vector. The Sb and O ions again have a coordination environment consistent with the α- and β-forms.

The calculated lattice parameters for all three forms are given in Table 1. Overall, there is quite a wide variation in the percentage error compared with experiment. For the α-phase, this error is 3.8%, which is greater than would normally be expected with the PBE methodology. Similarly, the lattice parameters for the γ-phase range between 3.9 and 4.5%. The β-phase, however, shows a greater anisotrophy, with the calculated *a* vector being 6.7% greater than experiment. In the β-phase, the Sb^{III} lone pairs are directed along the *a* vector and therefore are the likely cause of the discrepancy. Standard GGA methods are known to fail to model dispersion forces[77,78] without modification or a correction term added.[59,79−82] Therefore, a greater amount of uncertainty would be expected along the lattice vectors, which are dictated by these nonbonded interactions. The cubic crystal habit of α-Sb_2O_3 and the more complex structure of the γ-phase mean that this error is not constrained to a single vector, and all three vectors are seen to be overexpanded relative to experiment. The influence of the lack of dispersion forces is confirmed through the analysis of bond-length data, detailed in Table 2. For the α-form, the bond lengths are found to be more in-line with the experimental observation, being only 1.6% overestimated, despite the 3.8% overprediction of the lattice vector. Comparison of the smallest Sb−O inter- and intramolecular distances between and within the cages, respectively, further supports this. The intermolecular distances are seen to be 4.9% larger than experiment, while the error to experiment for the intramolecular distances is in-line with the bonded distances. This implies that while the unit cell is expanded relative to experiment, the bonding between Sn and O is reproduced well, with the expected small overestimation of PBE. A similar case is observed for β-Sb_2O_3, where the difference compared to the experimental bond lengths varies from 1.2 to 1.9% but the smallest error in the intermolecular Sb−O distance is 3.1% larger than experiment. For the γ-phase, a much larger variation in the cell vectors and bond lengths in comparison to

Table 1. Comparison between the Experimental Lattice Constants, Cell Volumes, and Formation Energies for Sb_2O_x (Where $x = 3$, 4, or 5) with Those Calculated Using a PBE Methodology[a]

material	property	PBE	experiment[74,76,83−85]
α-Sb_2O_3	a (Å)	11.533(3.8)	11.116
	volume (Å^3)	1534.01(11.7)	1373.55
	$\Delta E_{formation}$ (eV)	−6.68	−7.31
β-Sb_2O_3	a (Å)	5.008(6.7)	4.900
	b (Å)	12.654(1.8)	12.449
	c (Å)	5.527(2.2)	5.410
	volume (Å^3)	350.25(6.1)	330.01
	$\Delta E_{formation}$ (eV)	−6.74	
γ-Sb_2O_3	a (Å)	12.163(4.5)	11.641
	b (Å)	7.900(4.4)	7.567
	c (Å)	7.766(3.9)	7.477
	volume (Å^3)	326.05(5.1)	310.20
	$\Delta E_{formation}$ (eV)	−6.58	
α-Sb_2O_4	a (Å)	5.558(1.9)	5.452
	b (Å)	4.912(2.0)	4.818
	c (Å)	11.943(1.1)	11.808
	volume (Å^3)	326.05(5.1)	310.20
	$\Delta E_{formation}$ (eV)	−8.31	−9.28
β-Sb_2O_4	a (Å)	12.234(1.5)	12.057
	b (Å)	4.934(2.0)	4.835
	c (Å)	5.541(2.9)	5.384
	β (°)	76.931(2.0)	75.440
	volume (Å^3)	162.92(7.3)	151.90
	$\Delta E_{formation}$ (eV)	−8.30	
Sb_2O_5	a (Å)	12.87(1.8)	12.646
	b (Å)	4.893(2.3)	4.782
	c (Å)	5.525(1.8)	5.425
	β (°)	76.435(0.5)	76.090
	volume (Å^3)	347.98(6.1)	328.07
	$\Delta E_{formation}$ (eV)	−8.74	−10.17

experiment is observed, with the calculated bond lengths ranging from 10.8% smaller to 8.4% larger than experiment. This wide variation appears to result from a loss of asymmetry in the structure. In the calculated structure, the Sb−O bond distances are all similar, while the experimental structure shows a wider variation. Although the cause of this difference is not apparent, it may result from the poor description of the directional van der Waals in the symmetry.

The calculated formation energies for the three polymorphs suggest the order of stability is $\beta > \alpha > \gamma$, which is contrary to experimental evidence which reports that the α-phase is the most thermodynamically stable. This variation is likely a result of the lack of dispersion forces, which results in an overexpansion of the crystal structures causing the stability to be underpredicted relative to experiment. This underestimation will vary between the polymorphs, due to the different structural motifs, causing an incorrect trend to be predicted.

For the Sb^V oxide, Sb_2O_5, only one form is known, which has a monoclinic structure and crystallizes in the $C2/c$ space group, as shown in Figure 1f.[83,84] The Sb^V ions (Figure 1n) in the structure possess octahedral geometry, through bonding to six O atoms, which can be seen to form rutile-like layers when viewed along the [010] direction, highlighted by the polyhedra in Figure 1f. The O ions reside on two different crystallographic sites, 1 and 2, which are two- and three-coordinate, respectively. The character labels (a−c) in Figure 1n are used to indicate the different bonds that the two crystallographic sites can form. The calculated Sb_2O_5 structure has similar errors to experiment for all quantities (~2%), showing that the PBE methodology provides a good representation of the Sb_2O_5 structure.

Table 2. Calculated Bond Lengths, with Comparative Experimental Values, for Sb_2O_x (Where $x = 3$, 4, or 5)[a]

material	bonding pair	PBE	experiment[74,83−85]
α-Sb_2O_3	$Sb-O$	2.009(1.6)	1.978
	$Sb\cdots O_{intra}$	3.876(1.6)	3.815
	$Sb\cdots O_{inter}$	3.043	2.902
β-Sb_2O_3	$Sb-O_{1a}$	2.022(1.9)	1.984
	$Sb-O_{1b}$	2.045(1.2)	2.021
	$Sb-O_2$	2.059 (1.7)	2.024
	$Sb\cdots O_{intra}$	2.644(1.2)	2.612
	$Sb\cdots O_{inter}$	2.586(3.1)	2.507
γ-Sb_2O_3	Sb_1-O_1	2.000(−10.8)	2.239
	Sb_1-O_2	2.023(7.5)	1.882
	Sb_1-O_5	2.004(−2.4)	2.054
	Sb_2-O_1	2.030(8.4)	1.872
	Sb_2-O_4	2.003(4.9)	1.910
	Sb_2-O_6	2.005(−2.5)	2.080
	Sb_3-O_2	2.016(−4.5)	2.112
	Sb_3-O_3	2.049(0.5)	2.039
	Sb_3-O_4	2.003(−1.6)	2.035
	Sb_4-O_3	2.013(−3.2)	2.080
	Sb_4-O_5	2.000(−2.8)	2.055
	Sb_4-O_6	2.034(1.2)	2.013
α-Sb_2O_4	$Sb^{V}-O_{1a}$	2.052(−0.3)	2.058
	$Sb^{V}-O_{2a}$	2.028(1.7)	1.994
	$Sb^{V}-O_{3a}$	2.019(−4.4)	2.111
	$Sb^{V}-O_{3b}$	1.983(3.1)	1.924
	$Sb^{V}-O_{4a}$	2.002(3.5)	1.935
	$Sb^{V}-O_{4b}$	2.010(0.6)	1.998
	$Sb^{III}-O_{1b}$	2.218(−1.4)	2.249
	$Sb^{III}-O_{1c}$	2.076(3.1)	2.014
	$Sb^{III}-O_{2b}$	2.066(2.0)	2.026
	$Sb^{III}-O_{2c}$	2.269(0.4)	2.261
β-Sb_2O_4	$Sb^{V}-O_{1a}$	2.042(2.3)	1.997
	$Sb^{V}-O_{2a}$	2.042(2.3)	1.997
	$Sb^{V}-O_{3a}$	2.002(1.9)	1.965
	$Sb^{V}-O_{3b}$	2.008(2.1)	1.966
	$Sb^{V}-O_{4a}$	2.002(1.9)	1.965
	$Sb^{V}-O_{4b}$	2.008(2.1)	1.966
	$Sb^{III}-O_{1b}$	2.222(−0.8)	2.240
	$Sb^{III}-O_{1c}$	2.018(−2.3)	2.066
	$Sb^{III}-O_{2b}$	2.222(−0.8)	2.240
	$Sb^{III}-O_{2c}$	2.018(−2.3)	2.266
Sb_2O_5	$Sb-O_{1a}$	1.956(2.2)	1.913
	$Sb-O_{1b}$	1.931(2.0)	1.894
	$Sb-O_{1c}$	1.957(2.2)	1.915
	$Sb-O_{2a}$	2.141(1.9)	2.101
	$Sb-O_{2b}$	2.069(1.3)	2.043
	$Sb-O_{2c}$	2.14(2.7)	2.084

Diantimony tetroxide, Sb_2O_4, differs from the other two materials in that it has mixed valency, with both Sb^{III} and Sb^V oxidation states present. Two structural polymorphs exist, an orthorhombic α-phase (space group $Pna2_1$) and a monoclinic β-phase (space group $C2/c$). The α- to β-transformation occurs at a temperature of 935 °C but can also be induced through increased pressure.[85,86] The unit cells of the two polymorphs are given in Figure 1d,e, and the same basic structural motif is

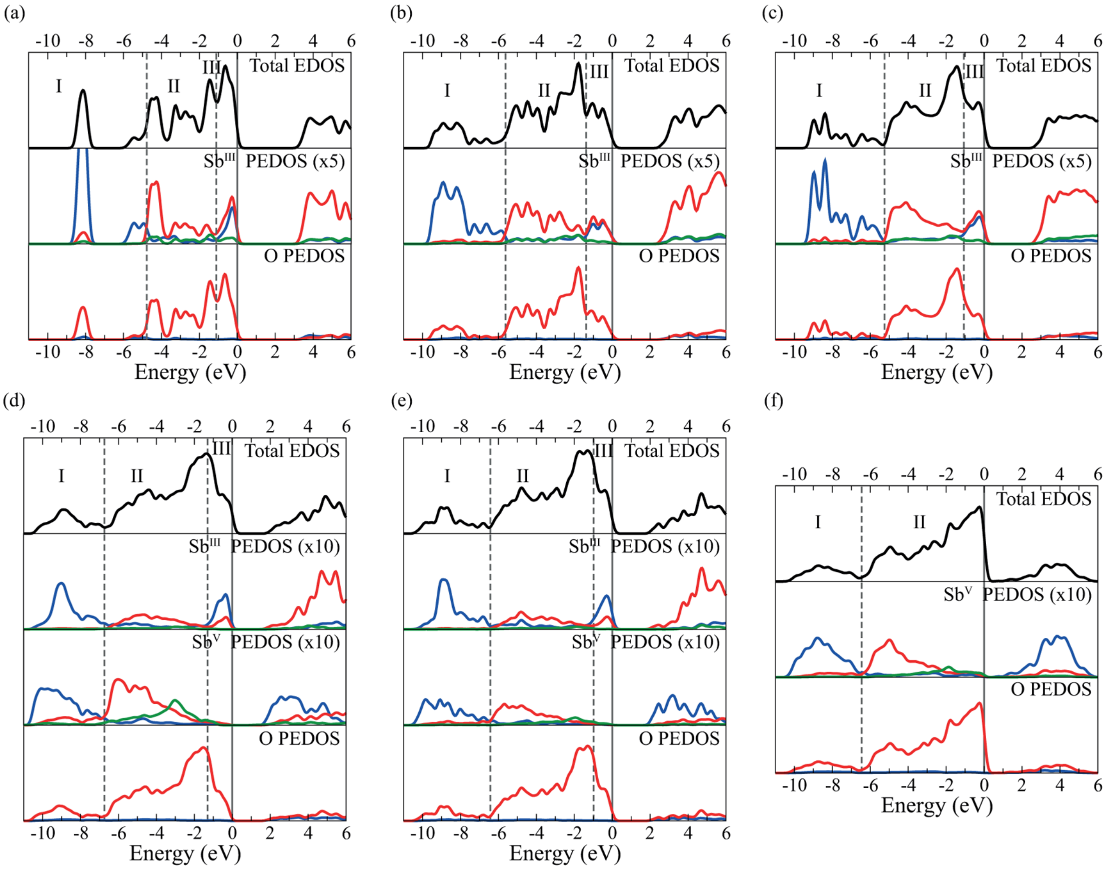

Figure 2. Calculated EDOS and PEDOS for (a) α-Sb_2O_3, (b) β-Sb_2O_3, (c) γ-Sb_2O_3, (d) α-Sb_2O_4, (e) β-Sb_2O_4, and (f) Sb_2O_5. The top of the valence band is set to 0.0 eV, indicated by the solid vertical line. The s, p, and d states are colored blue, red, and green, respectively.

observed for each form, albeit with the β-polymorph showing an increased symmetry in the Sb^{III} and Sb^{V} bonding environments. The structures possess layers of Sb^{III} and Sb^{V}, which alternate along one axis.[85] For the α-form, these are *ab* layers alternating along the *c* axis, whereas the β-polymorph possesses *bc* layers stacking along the *a* axis. The antimony ions have different coordination environments, depending on their oxidation states, as shown in Figure 1 j,l and k,m. The Sb^{III} atoms possess a distorted geometry to four O atoms, which form the bottom of a square-based pyramid. The site at the apex of the pyramid, which is directed along the *b* lattice vector, is vacant. The Sb^{V} atoms have a more regular, albeit slightly distorted, octahedral geometry. The O ions have two different coordination numbers within the structure, over four crystallographic sites. In Figure 1j,l and k,m, those labeled 1 and 2 have a trigonal planar geometry, bonding to two Sb^{III} ions and one Sb^{V} ion, whereas those designated as 3 and 4 are two-coordinate, bonding only to Sb^{V} ions. The character labels (*a*–*c*) in Figure 1j,l and k,m refer to the different bonds that the different crystallographic sites can form.

The calculated lattice parameters in Table 1 show that the structures are simulated at a similar level of accuracy, with the β-phase showing a slightly more expanded *c* vector. The calculated formation energies show a similar stability for the two polymorphs, likely influenced by dispersion forces resulting from the Sb^{III} ions. The calculated bond lengths for both forms have a large amount of variation when compared to experiment, ranging between −4.4 and 3.5% for the α-phase and between −2.3 and 2.3% for the β-phase. The variation in the α-form is caused by the simulated Sb^{V} octahedra being less distorted than those reported experimentally, possibly a result of the expanded *ab* plane. For the β-phase, the Sb^{III} bond lengths are all smaller than experiment, while the Sb^{V} bond lengths are larger.

Overall, the structures of all materials are reasonably well reproduced, with the discrepancies not significantly altering the structures or bond lengths. The presence of dispersive forces between Sb^{III} ions does cause some overestimation of lattice vectors, but the bond lengths are closer to experiment. Therefore, the bonding shown should be well described with the DFT methodology. The calculated formation energies are substantially underestimated, for a variety of reasons, although the trend in α-polymorphs is the same as observed experimentally.

Electronic Density of States. To assess the bonding characteristics of O with Sb^{III} and Sb^{V} atoms, the total (EDOS) and partial (*l*-quantum number- and ion-decomposed) electronic density of states (PEDOS) are given in Figure 2.

The valence band of α-Sb_2O_3, Figure 2a, can be split into three distinct regions based on composition. Region I, the bottom of the VB, contains a sharp peak, centered ~8 eV below the valence band maximum (VBM), which predominantly contains Sb 5s and O 2p states. A further Sb 5s doublet of peaks, with reduced intensity, is seen at the upper limit of this region. Region II is mainly composed of Sb 5p and O 2p states. The VBM, region III, is similar to region I, in that it contains a peak comprising Sb 5s and O 2p states; however, there is also a significant contribution from the Sb 5p states. The bottom of the conduction band is dominated by the unoccupied Sb p states. The α-Sb_2O_3 PEDOS is also consistent with the findings of Matsumoto et al.[41] The EDOS/PEDOS for the β- and γ-

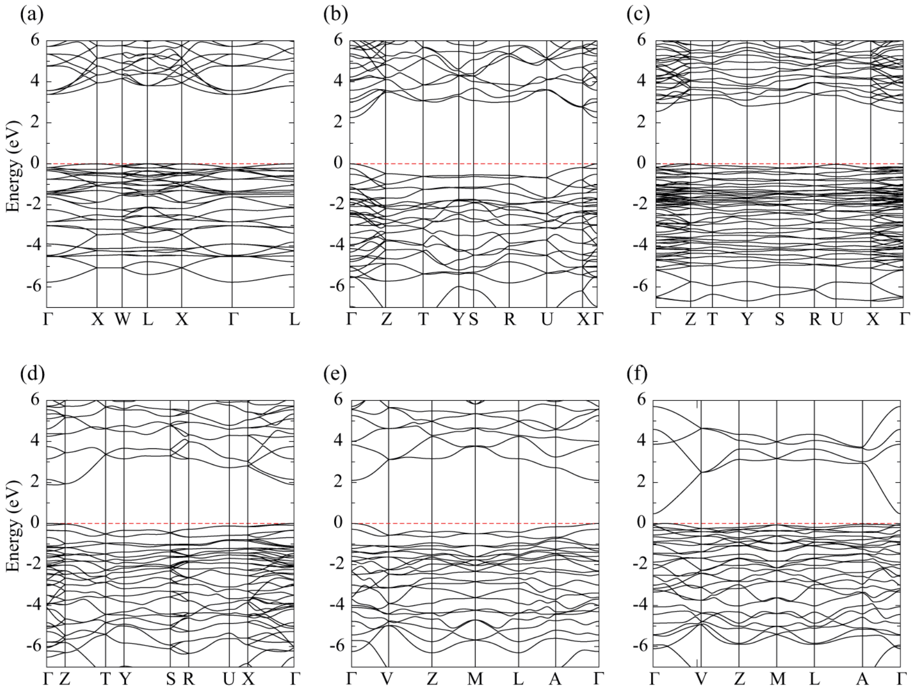

Figure 3. Calculated band structures of (a) α-Sb_2O_3, (b) β-Sb_2O_3, (c) γ-Sb_2O_3, (d) α-Sb_2O_4, (e) β-Sb_2O_4, and (f) Sb_2O_5, where the VBM is set to 0.0 eV, as indicated by the red dashed line.

polymorphs are similar in appearance to that of α-Sb_2O_3. A broadening and separation of peaks is observed due to the greater variation in Sb coordination environments, but regions of similar composition and location to I, II, and III can be identified, thus indicating similar bonding in the polymorphs.

In contrast to α-Sb_2O_3, the Sb_2O_5 valence band is better represented by 2 regions, which share similar characteristics with regions I and II of the α-Sb_2O_3 EDOS. Region I is again dominated by Sb 5s and O 2p states, although the Sb 5s states reside in a broad peak rather than the two sharp peaks seen for α-Sb_2O_3. Region II, however, contains the majority of contributions from the Sb 5p and O 2p states. Although, rather than being equally spread throughout the region, the Sb 5p states are mainly seen at the bottom of this region, with the peak centered ~5 eV below the VBM. The O 2p states dominate the upper region, reaching a maximum at the VBM. The bottom of the CB also differs from that of α-Sb_2O_3 as it has a greater proportion of unoccupied 5s states, thereby being more similar to region III of Sb_2O_3 than to its CB.

For α-Sb_2O_4, a separate PEDOS is presented for the Sb^{III} and Sb^{V} sites. The Sb^{III} PEDOS has a very similar composition to that of α-Sb_2O_3, and the VB can be split in three distinct regions. Regions I and III are again dominated by Sb 5s and O 2p states, with the latter region also showing a contribution from Sb 5p states. In comparison to α-Sb_2O_3, the VBM of α-Sb_2O_4 has a reduced amount of Sb 5p states. Similar comparisons can be made to Sb_2O_5 for the Sb^{V} ions. Region I contains the primary Sb 5s component, whereas region II (extending up to the VBM) contains the Sb 5p states. The Sb 5p peak, centered at −5.5 eV, diminishes on approaching the VBM, as the O 2p states increase, in a similar way to that for Sb_2O_5. The EDOS and PEDOS for β-Sb_2O_4 are very similar to that reported for the α-polymorph. The primary difference between the polymorphs, a reduction in the broadness of the peaks, results from the increased symmetry observed for the Sb coordination environments in the β-structure.

Band Structure and Optical Absorption. The band structures along the high symmetry lines[87] are shown for the different polymorphs in Figure 3. The α- and γ-Sb_2O_3 polymorphs are observed to have indirect fundamental band gaps of 3.38 and 2.55 eV. In the α-Sb_2O_3 band structure, the VBM is observed at the L-point, while the conduction band minimum (CBM) is present at Γ. The smallest direct fundamental gap of 3.54 eV is located offset from the Γ-point in the X-direction. For the γ-phase, the VBM is offset from the Z-point in the Γ-direction, while the CBM is observed at Γ with an energy of 2.55 eV. The smallest direct band fundamental gap is located at the Γ-point with an energy of 2.70 eV. The β-polymorph differs in that it is a direct band gap material, with a fundamental gap of 2.25 eV at the Γ-point. The polymorphs of Sb_2O_4 also show different natures, with the α-phase possessing a fundamental band gap which is indirect in nature, while the β-phase is a direct band gap material. For α-Sb_2O_4, the VBM is observed at the Γ-point, with the CBM offset from Γ toward the Z-point at an energy of 1.88 eV. The smallest direct band gap, observed at the CBM, however, is only marginally larger than the indirect gap, with an energy of 1.89 eV. The direct band gap of β-Sb_2O_4 is found at the Γ-point with a size of 2.10 eV. Finally, Sb_2O_5 possesses an indirect band gap, like the α-polymorphs. The VBM of Sb_2O_5 is located offset from the Γ-point in the V-direction, whereas the CBM is at Γ giving an indirect band gap of 0.47 eV. The smallest direct fundamental gap is observed at Γ with an energy of 0.53 eV.

The calculated optical absorption spectra for all polymorphs are plotted in Figure 4d. According to the Tauc relation, the optical band gap can be obtained by plotting $(\alpha h\nu)^2$ versus $h\nu$ and extrapolating $(\alpha h\nu)^2$ to zero, as described previously.[72] In this manner, we find optical band gaps of 3.54, 2.72, 2.90, 2.10, 2.24, and 0.76 eV for α-Sb_2O_3, β-Sb_2O_3, γ-Sb_2O_3, α-Sb_2O_4, β-Sb_2O_4, and Sb_2O_5, respectively. For each material, except β-Sb_2O_3, the onset of optical absorption occurs at the location of the smallest direct fundamental gap. However, as this initial

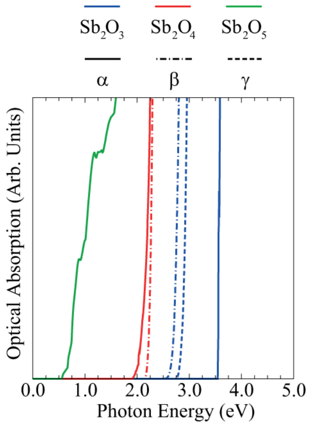

Figure 4. Calculated optical absorption spectra, $(\alpha h\nu)^2$, for Sb_2O_x (where $x = 3$, 4, or 5).

absorption is weak for the majority of materials, it results in the optical band gaps being slightly larger than the smallest direct gap. The direct gap for β-Sb_2O_3 is optically forbidden, so optical onset occurs from the second highest VB at the Γ-point to the CBM, rather than from the VBM, with an energy of 2.47 eV. Transitions from the third highest VB, with an energy of 2.76 eV, then cause the further increase in absorption and the resultant optical gap.

In comparison to previous work, Matsumoto et al.[41] quoted a calculated band gap of 3.33 eV for α-Sb_2O_3, using a similar PBE methodology, which is consistent with the indirect gap of this study, although they did not comment on whether it was direct or indirect in nature. Experimentally, optical gaps with a range of 3.4−4.0 eV[44,88] have been reported for thin films, with the gap observed to decrease with increasing film thickness and increasing temperature, stated as being the result of direct transitions. Conversely, an earlier study by Wood et al.[89] placed the optical gap at ∼4 eV and stated that it resulted from indirect transitions. As PBE calculations typically underestimate band gaps, this can be considered as reasonable agreement to experiment.

Although experimental data for the band gaps of the Sb_2O_4 polymorphs and Sb_2O_5 are lacking, it should be noted that the calculated value may be underestimated to a greater extent than Sb_2O_3. Previous PBE simulations on materials possessing a CB dominated by empty cation s states have often reported a significant underestimation of the band gap. For example, simulation of PbO_2 with a PBE methodology yields a metallic band structure, with an overlap of 0.7 eV at the Γ-point, while the use of a hybrid-DFT approach gives a gap at the same point of 0.35 eV.[90] Similar findings have been reported for SnO_2, with PBE giving a band gap of 0.6 eV but a hybrid-DFT study giving a value of 3.60 eV.[91,92] This is likely to have greater consequence for Sb_2O_5 but may also extend to the Sb_2O_4 polymorphs. Therefore, further simulation study and experimental evidence is need to clarify this issue.

Band-Edge Effective Masses. From a qualitative view, most of the antimony oxide structures have reasonably flat valence bands, suggesting that any p-type properties will likely be negligible. For the majority of the materials, the same can be assumed for the n-type properties from the bottom of the CBs. The CBM of Sb_2O_5, however, has a much greater curvature. Comparisons can be drawn with strong n-type materials such as In_2O_3[93] and CdO,[94] which both have highly dispersed CBMs due to the presence of empty cation s states. This indicates that it should also possess good n-type properties. To allow some quantitative analysis of this, the band-edge effective masses of holes and electrons at the VBM and CBM, respectively, have been determined for each material. The effective mass, m^*, is calculated by

$$\frac{1}{m^*} = \frac{1}{\hbar^2}\frac{d^2E}{dk^2} \tag{1}$$

where d^2E/dk^2 is obtained by a central difference between two points in the band structure, using the assumption that the dispersion is an even function about the band-edge in the given direction.[95] As the VBs of the three materials are clearly not parabolic in nature, they are not expected to be described well under a typical semiconductor effective mass approximation. However, as the CBs are more parabolic, the calculated electron effective masses should have a higher degree of accuracy than the hole effective masses. Regardless, the effective masses calculated using this method can serve as an approximate guide and allow some comparison to be made between the relative merits of the three structures for n/p-type conductivity, as has been done previously for other semiconductors.[69,71,93,96] The calculated hole and electron effective masses for each polymorph of Sb_2O_3, Sb_2O_4, and Sb_2O_5 are given in Table 3.

Table 3. Calculated Band-Edge Hole and Electron Effective Masses at the VBM and CBM for Sb_2O_x (Where x = 3, 4, or 5)[a]

material	hole effective mass	electron effective mass
α-Sb_2O_3	2.54 (Γ)	0.85 (L)
β-Sb_2O_3	0.63 (X)	0.39 (X)
γ-Sb_2O_3	1.33 (Z)	0.35 (Z)
α-Sb_2O_4	3.94 (X)	1.48 (Γ)
β-Sb_2O_4	2.99 (V)	1.52 (V)
Sb_2O_5	1.11 (V)	0.19 (A)

The hole effective masses for the α- and γ-Sb_2O_3 polymorphs indicate that the p-properties are likely to be poor. For comparison, the experimental hole effective mass for Cu_2O, a reasonable p-type material, is 0.56 m_e.[97] The α- and γ-polymorphs also possess other maxima in the valence band which are close in energy to the VBMs. For α-Sb_2O_3, a hole effective mass of 2.20 m_e is found at X in the W-direction, while for γ-Sb_2O_3, U has an effective mass of 1.34 m_e in the R-direction. Therefore, no significant p-type conductivity would be expected to result from these points. For β-Sb_2O_4, a hole effective mass of 0.63 m_e is observed in the X-direction, indicating that this may exhibit reasonable p-type properties which are superior to the other polymorphs. In comparison to the hole effective masses, the electron effective masses indicate that the n-type properties are likely to be stronger. The strong n-type conductors In_2O_3 and CdO have calculated electron effective masses of 0.24[93] and 0.21 m_e,[94] respectively. Therefore, while the different Sb_2O_3 polymorphs are not expected to show exceptional n-type conductivity either, the β- and γ-phases show promise and may warrant further examination.

The polymorphs of Sb_2O_4 exhibit similar band-edge effective masses; however, neither structure is expected to show strong conductivity properties via either mechanism. Sb_2O_5 also shows a large hole effective mass, indicative of poor p-type conduction. The topmost valence band of Sb_2O_5 also has two other maxima which are close in energy to the VBM (at M and

A); however, they both possess larger hole effective masses, and therefore, they are not expected to compete with any p-type conductivity mechanism. In contrast to the poor p-type properties, the curvature of the conduction band suggests that the n-type conductivity should be more significant. The electron effective mass is comparable to that observed in materials like In_2O_3 and CdO and is, therefore, sufficiently low as to warrant further investigation via experiment.

■ DISCUSSION

The structures of the three antimony oxides, Sb_2O_3, Sb_2O_4, and Sb_2O_5, clearly show that the Sb^{III} sites are more distorted than those containing Sb^{V} ions. Corresponding differences are also observed in the calculated PEDOSs between the oxidation states (Figure 2). This is particularly apparent at the VBM; both species show an O 2p component, but the Sb^{III} ions show an additional Sb 5s/p contribution. To understand these differences, it is instructive to consider the charge density. The partial charge density at the top of the VB (−2.0 to 0.0 eV) for each of the three materials is shown in Figure 5. Due to the similarity in the PEDOSs, partial density is only shown for the α-polymorphs of Sb_2O_3 and Sb_2O_4. Asymmetric density is clearly visible on the Sb^{III} ions in α-Sb_2O_3 and α-Sb_3O_4, yet absent for Sb^{V} ions in α-Sb_2O_4 and Sb_2O_5. Furthermore, the asymmetric density is slightly stronger for α-Sb_2O_3. This correlates the Sb states at the VBM with the observed asymmetric density.

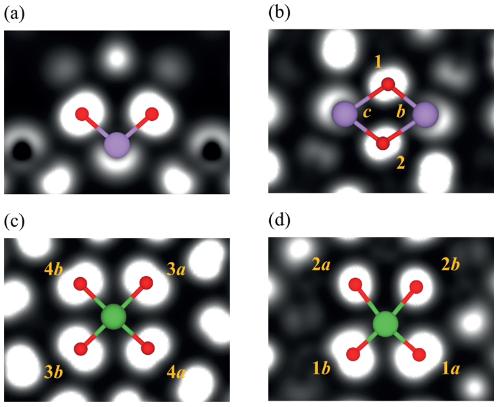

Figure 5. Calculated partial charge density plots over −2.0 to 0.0 eV of the EDOS for Sb^{III} atoms in (a) α-Sb_2O_3 and (b) α-Sb_2O_4, and Sb^{V} atoms in (c) α-Sb_2O_4 and (d) Sb_2O_5. Contours vary from 0.00 (black) to 0.17 electrons $Å^{-3}$ (white). Atoms labels (orange) correspond to those given in Figure 1.

In previous work on the Sn monochalcogenides, Walsh and Watson[28] used analysis from crystal orbital overlap populations to further characterize this type of interaction. They found that the region at the bottom of the VB (region I for Sb^{III} ions in Figure 2), which was composed primarily of Sn 5s and anion p states, corresponded to a bonding interaction between these species. The region at the top of the VB (region III for Sb^{III} ions in Figure 2), which has a similar composition but with the addition of cation p states, was found to be an antibonding interaction. From this, we can thus conclude that regions I and III in the EDOSs of this study also most likely correspond to Sb−O bonding and antibonding interactions, respectively. The antibonding character of region III (for α-Sb_2O_3 and α-Sb_2O_4) ions is also consistent with the charge density between Sb^{III} and O ions going to zero in Figure 5. Overall, this indicates that the Sb^{III} lone pair is formed in a similar manner to other materials, which have a oxidation state of two lower than the group valence.

The reduced Sb 5p contribution to the α-Sb_2O_4 VBM, relative to α-Sb_2O_3, indicates that the antibonding orbital is stabilized to a lesser extent, leading to a weaker lone pair. This correlates with the charge density plots, where the asymmetric density of α-Sb_2O_4 was observed to be reduced relative to α-Sb_2O_3. The reduced interaction of the Sb 5p states is likely due to the presence of the Sb^{V} ions. The regular octahedral coordination of these ions in α-Sb_2O_4 acts to constrain the geometry around the Sb^{III} ions away from that which would maximize the lone-pair interaction. This indicates the importance of the atomic coordination on the strength and formation of the asymmetric density in these systems.

■ CONCLUSION

This study has used DFT calculations to characterize the electronic structure of the three binary oxides of antimony. Through the analysis of calculated PEDOSs and charge density plots, the difference in bonding of oxygen with Sb^{III} and Sb^{V} ions is determined, as well as the chemical origin of the Sb^{III} lone pair. The results show that the formation of asymmetric density, or lone pairs, on Sb^{III} ions is achieved in a similar manner as for other main group cations which exhibit an oxidation state of two lower than the group valence. The lone pair does not consist of a chemically inert yet stereochemically active sp hybrid orbital but through direct chemical interaction between Sb s and O p states, with the antibonding component stabilized by the cation p states. This interaction is facilitated by the structural distortion observed around Sb^{III} ions.

The calculated band structures indicate that all three materials possess indirect fundamental band gaps, with values of 3.38, 1.88, and 0.47 eV for α-SbO_3, α-Sb_2O_4, and Sb_2O_5, respectively. For Sb_2O_3, both the β- and γ-polymorphs show reduced band gaps to the α-form, with fundamental gaps of 2.25 and 2.55, respectively. The band gap for β-Sb_2O_3 differs in that it is direct in nature though. For Sb_2O_4, the β-form shows a slightly increased band gap of 2.10 eV, which is also direct in nature. The VBM of β-Sb_2O_3 possesses a relatively small hole effective mass, and therefore, it may also show reasonable p-type properties. In addition, the CBMs of β-Sb_2O_3, γ-Sb_2O_3 , and Sb_2O_5 all show an increased amount of curvature with small calculated electron effective masses, suggesting that they may exhibit strong n-type properties. These materials are, therefore, highlighted for possible future study to further elucidate their electrical properties.

Optical absorption spectra have also been calculated for all polymorphs. With the exception of β-Sb_2O_3, the optical band gaps result from the smallest direct fundamental gaps (3.54, 2.70, 1.89, 2.10, and 0.53 eV for α-Sb_2O_3, γ-Sb_2O_3, α-Sb_2O_4, β-Sb_2O_4, and Sb_2O_5, respectively). The onset of optical absorption for all except α-Sb_2O_3 is weak though, resulting in the optical gaps being slightly larger than the smallest direct gaps (3.54, 2.90, 2.10, 2.24, and 0.76, respectively). For β-Sb_2O_3, the direct gap is optically forbidden, so the optical gap results from transitions between the second and third highest VBs and the CBM, giving an increased optical band gap of 2.72 eV.

■ AUTHOR INFORMATION

Corresponding Author

*E-mail: allenje@tcd.ie; watsong@tcd.ie.

Notes

The authors declare no competing financial interest.

■ ACKNOWLEDGMENTS

This work was supported by Science Foundation Ireland through the Principal Investigators program (PI Grant Numbers 06/IN.1/I92 and 06/IN.1/I92/EC07). Calculations were performed on the Lonsdale supercomputer, as maintained by TCHPC, and the Stokes supercomputer, as maintained by ICHEC. D.O.S. is grateful to the Ramsay Memorial Trust and University College London for the provision of a Ramsay Fellowship. D.O.S. and A.W. acknowledge membership of the Materials Design Network.

■ REFERENCES

(1) Galip, H.; Hasipoğlu, H.; Gündüz, G. Flame-Retardant Polyester. *J. Appl. Polym. Sci.* **1999**, *74*, 2906−2910.

(2) Weil, E. D.; Levchik, S.; Moy, P. Flame and Smoke Retardants in Vinyl Chloride Polymers—Commercial Usage and Current Developments. *J. Fire Sci.* **2006**, *24*, 211−236.

(3) Brebu, M.; Jakab, E.; Sakata, Y. Effect of Flame Retardants and Sb_2O_3 Synergist on the Thermal Decomposition of High-Impact Polystyrene and on Its Debromination by Ammonia Treatment. *J. Anal. Appl. Pyrolysis* **2007**, *79*, 346−352.

(4) Youk, J. H.; Kambour, R. P.; MacKnight, W. J. Polymerization of Ethylene Terephthalate Cyclic Oligomers with Antimony Trioxide. *Macromolecules* **2000**, *33*, 3594−3599.

(5) Gilliam, S. J.; Jensen, J. O.; Banerjee, A.; Zeroka, D.; Kirkby, S. J.; Merrow, C. N. A Theoretical and Experimental Study of Sb_4O_6: Vibrational Analysis, Infrared and Raman Spectra. *Spectrochim. Acta, Part A* **2004**, *60*, 425−434.

(6) Gaigneaux, E. M.; Ruiz, P.; Delmon, B. Further on the Mechanism of the Synergy between MoO_3 and α-Sb_2O_4 in the Selective Oxidation of Isobutene to Methacrolein: Reconstruction of MoO_3 via Spillover Oxygen. *Catal. Today* **1996**, *32*, 37−46.

(7) Nilsson, J.; Landa-Cánovas, A.; Hansen, S.; Andersson, A. Catalysis and Structure of the $SbVO_4/Sb_2O_4$ System for Propane Ammoxidation. *Catal. Today* **1997**, *33*, 97−108.

(8) Díaz, R.; Mann, R. S. ESR and FTIR Spectroscopy Study of Sb−Mo Oxide Catalysts. *Mater. Lett.* **1997**, *33*, 19−22.

(9) Shishido, T.; Inoue, A.; Konishi, T.; Matsuura, I.; Takehira, K. Oxidation of Isobutane over Mo−V−Sb Mixed Oxide Catalyst. *Catal. Lett.* **2000**, *68*, 215−221.

(10) Huang, Y.; Ruiz, P. The Nature of Antimony-Enriched Surface Layer of Fe−Sb Mixed Oxides. *Appl. Surf. Sci.* **2006**, *252*, 7849−7855.

(11) Matsumura, H.; Okumura, K.; Shimamura, T.; Ikenaga, N. O.; Miyake, T.; Suzuki, T. Selective Oxidation of Methane to Formaldehyde over Antimony Oxide-Loaded Catalyst. *J. Mol. Catal. A* **2006**, *250*, 122−130.

(12) Asryan, N. A.; Alikhanyan, A. S.; Nipan, G. D. p-T-x Phase Diagram of the Sb−O System. *Inorg. Mater.* **2004**, *40*, 720−725.

(13) Chen, X.; Chen, G. Stable Ti/RuO_2−Sb_2O_5−SnO_2 Electrodes for O_2 Evolution. *Electrochim. Acta* **2005**, *50*, 4155−4159.

(14) Haverkamp, R. G.; Marshall, A. T.; Cowie, B. C. C. Energy Resolved XPS Depth Profile of (IrO_2, RuO_2, Sb_2O_5, SnO_2) Electrocatalyst Powder to Reveal Core−Shell Nanoparticle Structure. *Surf. Interface Anal.* **2011**, *43*, 847−855.

(15) Koivula, R. The Effect of Dopant's Valence (+III and +V) on the Anion/Cation Uptake Properties of Antimony-Doped Tin Dioxide. *Cent. Eur. J. Chem.* **2010**, *8*, 1179−1184.

(16) Zhang, D.; Tao, L.; Deng, Z.; Zhang, J.; Chen, L. Surface Morphologies and Properties of Pure and Antimony-Doped Tin Oxide Films Derived by Sol−Gel Dip-Coating Processing. *Mater. Chem. Phys.* **2006**, *100*, 275−280.

(17) Samanta, K.; Bhattacharya, P.; Katiyar, R. S. Raman Scattering Studies of p-Type Sb-Doped ZnO Thin Films. *J. Appl. Phys.* **2010**, *108*, 113501.

(18) Sidgwick, N. V. *The Electronic Theory of Valency*; Clarendon Press: Oxford, U.K., 1927.

(19) Gillespie, R. J.; Nyholm, R. S. Inorganic Stereochemistry. *Q. Rev. Chem. Soc.* **1957**, *11*, 339−380.

(20) Orgel, L. E. The Stereochemistry of *B* Subgroup Metals. Part II. The Inert Pair Effect. *J. Chem. Soc.* **1959**, 3815−3819.

(21) Lefebvre, I.; Lannoo, M.; Allan, G.; Ibanez, A.; Fourcade, J.; Jumas, J. C.; Beaurepaire, E. Electronic Properties of Antimony Chalcogenides. *Phys. Rev. Lett.* **1987**, *59*, 2471−2474.

(22) Olivier-Fourcade, J.; Ibanez, A.; Jaumas, J. C.; Maurin, M.; Lefebvre, I.; Lippens, P.; Lannoo, M.; Allan, G. Chemical Bonding and Electronic Properties in Antimony Chalcogenides. *J. Solid State Chem.* **1990**, *87*, 366−377.

(23) Watson, G. W.; Parker, S. C. Origin of the Lone Pair of α-PbO from Density Functional Theory Calculations. *J. Phys. Chem. B* **1999**, *103*, 1258−1262.

(24) Watson, G. W.; Parker, S. C.; Kresse, G. Ab Initio Calculation of the Origin of the Distortion of α-PbO. *Phys. Rev. B* **1999**, *59*, 8481−8486.

(25) Watson, G. W. The Origin of the Electron Distribution in SnO. *J. Chem. Phys.* **2001**, *114*, 758−763.

(26) Waghmare, U. V.; Spaldin, S. A.; Kandpal, H. C.; Seshadri, R. First-Principles Indicators of Metallicity and Cation Off-Centricity in the IV−VI Rocksalt Chalcogenides of Divalent Ge, Sn, and Pb. *Phys. Rev. B* **2003**, *67*, 125111.

(27) Walsh, A.; Watson, G. W. The Origin of the Stereochemically Active Pb(II) Lone Pair: DFT Calculations on PbO and PbS. *J. Solid State Chem.* **2005**, *178*, 1422−1428.

(28) Walsh, A.; Watson, G. W. Influence of the Anion on Lone Pair Formation in Sn(II) Monochalcogenides: A DFT Study. *J. Phys. Chem. B* **2005**, *109*, 18868−18875.

(29) Payne, D. J.; Egdell, R. G.; Walsh, A.; Watson, G. W.; Guo, J. H.; Glans, P. A.; Learmonth, T.; Smith, K. E. Electronic Origins of Structural Distortions in Post-Transition Metal Oxides: Experimental and Theoretical Evidence for a Revision of the Lone Pair Model. *Phys. Rev. Lett.* **2006**, *96*, 157403.

(30) Payne, D. J.; Egdell, R. G.; Law, D. S. L.; Glans, P. A.; Learmonth, T.; Smith, K. E.; Guo, J. H.; Walsh, A.; Watson, G. W. Experimental and Theoretical Study of the Electronic Structure of α-PbO and β-PbO_2. *J. Mater. Chem.* **2007**, *17*, 267−277.

(31) Walsh, A.; Payne, D. J.; Egdell, R. G.; Watson, G. W. Stereochemistry of Post-Transition Metal Oxides: Revision of the Classical Lone Pair Model. *Chem. Soc. Rev.* **2011**, *40*, 4455−4463.

(32) Walsh, A.; Watson, G. W.; Payne, D. J.; Edgell, R. G.; Guo, J.; Glans, P. A.; Learmonth, T.; Smith, K. E. Electronic Structure of the α and δ phases of Bi_2O_3: A Combined Ab Initio and X-ray Spectroscopic Study. *Phys. Rev. B* **2006**, *73*, 235104.

(33) Seshadri, R.; Hill, N. A. Visualizing the Role of Bi 6s "Lone Pair" in the Off-Center Distortion in Ferromagnetic $BiMnO_3$. *Chem. Mater.* **2001**, *13*, 2892−2899.

(34) Yang, J.; Dolg, M. Computational Investigation of the Bi-Lone-Pairs in Monoclinic Bismuth Triborate BiB_3O_6. *Phys. Chem. Chem. Phys.* **2007**, *9*, 2094−2102.

(35) Seshadri, R.; Baldinozzi, G.; Felser, C.; Tremel, W. Visualizing Electronic Structure Changes Across an Antiferromagnetic Phase Transition: Pb_2MgWO_6. *J. Mater. Chem.* **1999**, *9*, 2463−2466.

(36) Seshadri, R. Visualizing Lone Pairs in Compounds Containing Heavier Congeners of the Carbon and Nitrogen Group Elements. *Proc.—Indian Acad. Sci., Chem. Sci.* **2001**, *113*, 487−496.

(37) Raulot, J.-M.; Baldinozzi, G.; Seshadri, R.; Cortona, P. An Ab Initio Study of the Role of Lone Pairs in the Structure and Insulator-Metal Transition in SnO and PbO. *Solid State Sci.* **2002**, *4*, 467−474.

(38) Seshadri, R. Lone Pairs in Insulating Pyrochlores: Ice Rules and High-*k* Behavior. *Solid State Sci.* **2006**, *8*, 259−266.

(39) Stoltzfus, M. W.; Woodward, P. M.; Seshadri, R.; Klepeis, J.-H.; Bursten, B. Structure and Bonding in $SnWO_4$, $PbWO_4$ and $BiVO_4$: Lone Pairs vs Inert Pairs. *Inorg. Chem.* **2007**, *46*, 3839−3850.

(40) Rodriguez, E. E.; Poineau, F.; Llobet, A.; Czerwinski, K.; Seshadri, R.; Cheetham, A. K. Preparation and Crystal Structures of

Bismuth Technetates: A New Metal Oxide System. *Inorg. Chem.* **2008**, *47*, 6281−6288.

(41) Matsumoto, A.; Koyama, A.; Togo, A.; Choi, M.; Tanaka, I. Electronic Structures of Dynamically Stable As_2O_3, Sb_2O_3, and Bi_2O_3 Crystal Polymorphs. *Phys. Rev. B* **2011**, *83*, 214110.

(42) Kaiser, B.; Bernhardt, T. M.; Kinne, M.; Rademann, K.; Heidenreich, A. Formation, Stability, and Structures of Antimony Oxide Cluster Ions. *J. Chem. Phys.* **1999**, *110*, 1437−1449.

(43) Tigau, N. Structure and Electrical Conduction of Sb_2O_3 Thin Films. *Cryst. Res. Technol.* **2006**, *41*, 1106−1111.

(44) Tigau, N.; Ciupina, V.; Prodan, G. Structural, Optical and Electrical Properties of Sb_2O_3 Thin Films with Different Thickness. *J. Optoelectron. Adv. Mater.* **2006**, *8*, 37−42.

(45) Pereira, A. L. J.; Gracia, L.; Santamaría-Pérez, D.; Vilaplana, R.; Manjón, F. J.; Errandonea, D.; Nalin, M.; Beltrán, A. Structural and Vibrational Study of Cubic Sb_2O_3 under High Pressure. *Phys. Rev. B* **2012**, *85*, 174108.

(46) Cody, C. A.; DiCarlo, L.; Darlington, R. K. Vibrational and Thermal Study of Antimony Oxides. *Inorg. Chem.* **1979**, *18*, 1572−1576.

(47) Mestl, G.; Ruiz, P.; Delmon, B.; Knözinger, H. Sb_2O_3/Sb_2O_4 in Reducing/Oxidizing Environments: An In Situ Raman Spectroscopy Study. *J. Phys. Chem.* **1994**, *98*, 11276−11282.

(48) Naidu, B. S.; Pandey, M.; Sudarsan, V.; Vatsa, R. K.; Tewari, R. Photoluminescence and Raman Spectroscopic Investigations of Morphology Assisted Effects in Sb_2O_3. *Chem. Phys. Lett.* **2009**, *474*, 180−184.

(49) Amador, J.; Puebla, E. G.; Monge, M. A.; Rasines, I.; Valero, C. R. Diantimony Tetraoxides Revisited. *Inorg. Chem.* **1988**, *27*, 1367−1370.

(50) Moore, E. A.; Widatallah, H. M. Iron(III) as a Defect in Diantimony Tetroxide. *Mater. Res. Bull.* **2008**, *43*, 2361−2367.

(51) Teller, R. G.; Antonio, M. R.; Brazdil, J. F.; Grasselli, R. K. New Materials Synthesis: Characterization of Some Metal-Doped Antimony Oxides. *J. Solid State Chem.* **1986**, *64*, 249−260.

(52) Du, J.; Ji, Z.; Wang, C. The Effect of Doping by IV-Family Elements on the Electronic Structure and Electrical Characteristics of Sb_2O_5. *Cent. Eur. J. Phys.* **2007**, *5*, 103−109.

(53) Kresse, G.; Hafner, J. Ab Initio Molecular-Dynamics Simulation of the Liquid-Metal-Amorphous-Semiconductor Transition in Germanium. *Phys. Rev. B* **1994**, *49*, 14251−14271.

(54) Kresse, G.; Furthmüller, J. Efficient Iterative Schemes for Ab Initio Total-Energy Calculations Using a Plane-Wave Basis Set. *Phys. Rev. B* **1996**, *54*, 11169−11186.

(55) Perdew, J. P.; Burke, K.; Ernzerhof, M. Generalized Gradient Approximation Made Simple. *Phys. Rev. Lett.* **1996**, *77*, 3865−3868.

(56) Blöchl, P. E. Projector Augmented-Wave Method. *Phys. Rev. B* **1994**, *50*, 17953−17979.

(57) Kresse, G.; Joubert, D. From Ultrasoft Pseudopotentials to the Projector Augmented-Wave Method. *Phys. Rev. B* **1999**, *59*, 1758−1775.

(58) Murnaghan, F. D. The Compressibility of Media under Extreme Pressures. *Proc. Natl. Acad. Sci. U.S.A.* **1944**, *30*, 244−247.

(59) Allen, J. P.; Scanlon, D. O.; Parker, S. C.; Watson, G. W. Tin Monoxide: Structural Prediction from First Principles Calculations with van der Waals Corrections. *J. Phys. Chem. C* **2011**, *115*, 19916−19924.

(60) Monkhorst, H. J.; Pack, J. D. Special Points for Brillouin-Zone Integration. *Phys. Rev. B* **1976**, *13*, 5188−5192.

(61) *CRC Handbook of Chemistry and Physics*, 79th Edition; Lide, D. R., Ed.; CRC Press: Boca Raton, FL, 1998.

(62) Curtiss, L. A.; Raghavachari, K.; Redfern, P. C.; Pople, J. A. Assessment of Gaussian-2 and Density Functional Theories for the Computation of Enthalpies of Formation. *J. Chem. Phys.* **1997**, *106*, 1063−1079.

(63) Morgan, B. J.; Watson, G. W. A DFT+*U* Description of Oxygen Vacancies at the TiO_2 Rutile (110) Surface. *Surf. Sci.* **2007**, *601*, 5034−5041.

(64) Gajdos, M.; Hummer, K.; Kresse, G.; Furthmüller, J.; Bechstedt, F. Linear Optical Properties in the Projector-Augmented Wave Methodology. *Phys. Rev. B* **2006**, *73*, 045112.

(65) Adolph, B.; Furthmüller, J.; Beckstedt, F. Optical Properties of Semiconductors Using Projector-Augmented Waves. *Phys. Rev. B* **2001**, *63*, 125108.

(66) Ramos, L. E.; Paier, J.; Kresse, G.; Bechstedt, F. Optical Spectra of Si Nanocrystallites: Bethe-Salpeter Approach versus Time-Dependent Density-Functional Theory. *Phys. Rev. B* **2008**, *78*, 195423.

(67) Paier, J.; Marsman, M.; Kresse, G. Dielectric Properties and Excitons for Extended Systems from Hybrid Functionals. *Phys. Rev. B* **2008**, *78*, 121201.

(68) Nie, X.; Wei, S. H.; Zhang, S. B. Bipolar Doping and Band-Gap Anomalies in Delafossite Transparent Conductive Oxides. *Phys. Rev. Lett.* **2002**, *88*, 066405.

(69) Scanlon, D. O.; Watson, G. W. $(Cu_2S_2)(Sr_3Sc_2O_5)$-A Layered, Direct Band Gap, p-Type Transparent Conducting Oxychalcogenide: A Theoretical Analysis. *Chem. Mater.* **2009**, *21*, 5435−5442.

(70) Kehoe, A. B.; Scanlon, D. O.; Watson, G. W. Nature of the Band Gap of Tl_2O_3. *Phys. Rev. B* **2011**, *83*, 233202.

(71) Allen, J. P.; Nilsson, M. K.; Scanlon, D. O.; Watson, G. W. Comparison of the Defective Pyrochlore and Ilmenite Polymorphs of $AgSbO_3$ Using GGA and Hybrid DFT. *Phys. Rev. B* **2011**, *83*, 035207.

(72) Allen, J. P.; Scanlon, D. O.; Watson, G. W. Electronic Structures of Silver Oxides. *Phys. Rev. B* **2011**, *84*, 115141.

(73) Momma, K.; Izumi, F. VESTA 3 for Three-Dimensional Visualization of Crystal, Volumetric, and Morphology Data. *J. Appl. Crystallogr.* **2011**, *44*, 1272−1276.

(74) Whitten, A. E.; Dittrich, B.; Spackman, M. A.; Turner, P.; Brown, T. C. Charge Density Analysis of Two Polymorphs of Antimony(III) Oxide. *Dalton Trans.* **2004**, *1*, 23−29.

(75) Orman, R. G.; Holland, D. Thermal Phase Transitions in Antimony (III) Oxides. *J. Solid State Chem.* **2007**, *180*, 2587−2596.

(76) Orosel, D.; Dinnebier, R. E.; Blatov, V. A.; Jansen, M. Structure of a New High-Pressure−High-Temperature Modification of Antimony (III) Oxide, γ-Sb_2O_3, From High-Resolution Synchrotron Powder Diffraction Data. *Acta Crystallogr.* **2012**, *B68*, 1−7.

(77) Koch, W.; Jan Baerends, E.; Holthausen, M. C. *A Chemist's Guide to Density Functional Theory*; Wiley-VCH Verlag GmbH: Weinheim, Germany, 2001.

(78) Wu, Q.; Yang, W. Empirical Correction to Density Functional Theory for van der Waals Interactions. *J. Chem. Phys.* **2002**, *116*, 515−524.

(79) Dobson, J. F.; McLennan, K.; Rubio, A.; Wang, J.; Gould, T.; Le, H. M.; Dinte, B. P. Prediction of Dispersion Forces: Is There a Problem? *Aust. J. Chem.* **2001**, *54*, 513−527.

(80) Dion, M.; Ryberg, H.; Schröder, E.; Langreth, D. C.; Lundqvist, B. I. Van der Waals Density Functional for General Geometries. *Phys. Rev. Lett.* **2004**, *92*, 246401.

(81) Grimme, S.; Antony, J.; Ehrlich, S.; Krieg, H. A Consistent and Accurate Ab Initio Parameterization of Density Functional Dispersion Correction (DFT-D) for the 94 Elements H-Pu. *J. Chem. Phys.* **2010**, *132*, 154104.

(82) Quackenbush, N. F.; Allen, J. P.; Scanlon, D. O.; Sallis, S.; Hewlett, J. A.; Nandur, A. S.; Chen, B.; Smith, K. E.; Weiland, C.; Fischer, D. A.; Woicik, J.; White, B. E.; Watson, G. W.; Piper, L. F. J. Origin of the Bipolar Doping Behaviour of SnO from X-ray Spectroscopy and Density Functional Theory. *Chem. Mater.* **2013**, DOI: 10.1021/cm401343a.

(83) Jansen, M. Kristallstruktur von Sb_2O_5. *Angew. Chem.* **1978**, *90*, 141−142.

(84) Jansen, M. Crystal Structure of Sb_2O_5. *Angew. Chem., Int. Ed. Engl.* **1978**, *17*, 137−137.

(85) Orosel, D.; Balog, P.; Liu, H.; Qian, J.; Jansen, M. Sb_2O_4 at High Pressures and High Temperatures. *J. Solid State Chem.* **2005**, *178*, 2602−2607.

(86) Teller, R. G.; Antonio, M. R.; Brazdil, J. F.; Mehicic, M.; Grasselli, R. K. Stabilization of High-Temperature Antimony Oxide with Molybdenum Incorporation, Structure of Mo-Doped Sb_2O_4 by

Powder Neutron Diffraction and Extended X-ray Absorption Fine Structure Spectroscopy. *Inorg. Chem* **1985**, *24*, 3370−3375.

(87) Bradley, C. J.; Cracknell, A. P. *Mathematical Theory of Symmetry in Solids*; Oxford University Press: Oxford, U.K., 1972.

(88) Tigau, N.; Ciupina, V.; Prodan, G. The Effect of Substrate Temperature on the Optical Properties of Polycrystalline Sb_2O_3 Thin Films. *J. Cryst. Growth* **2005**, *277*, 529−535.

(89) Wood, C.; van Pelt, B.; Dwight, A. The Optical Properties of Amorphous and Crystalline Sb_2O_3. *Phys. Status Solidi B* **1972**, *54*, 701−706.

(90) Scanlon, D. O.; Kehoe, A. B.; Watson, G. W.; Jones, M. O.; David, W. I. F.; Payne, D. J.; Egdell, R. G.; Edwards, P. P.; Walsh, A. Nature of the Band Gap and Origin of the Conductivity of PbO_2 Revealed by Theory and Experiment. *Phys. Rev. Lett.* **2011**, *107*, 246402.

(91) Godinho, K. G.; Walsh, A.; Watson, G. W. Energetic and Electronic Structure Analysis of Intrinsic Defects in SnO_2. *J. Phys. Chem. C* **2008**, *113*, 439−448.

(92) Scanlon, D. O.; Watson, G. W. On the Possibility of p-Type SnO_2. *J. Mater. Chem.* **2012**, *22*, 25236−25245.

(93) Walsh, A.; Da Silva, J. L. F.; Wei, S. H. Origins of Band-Gap Renormalization in Degenerately Doped Semiconductors. *Phys. Rev. B* **2008**, *78*, 075211.

(94) Burbano, M.; Scanlon, D. O.; Watson, G. W. Sources of Conductivity and Doping Limits in CdO from Hybrid Density Functional Theory. *J. Am. Chem. Soc.* **2011**, *133*, 15065−15072.

(95) Kittel, C. *Introduction to Solid State Physics*, 7th ed.; John Wiley & Sons, Inc.: New York, 1996.

(96) Scanlon, D. O.; Godinho, K. G.; Morgan, B. J.; Watson, G. W. Understanding Conductivity Anomalies in for Cu^I-Based Delafossite Transparent Conducting Oxides: Theoretical Insights. *J. Chem. Phys.* **2010**, *132*, 024707.

(97) Hodby, J. W.; Jenkins, T. E.; Schwab, C.; Tamura, H.; Trivich, D. Cyclotron Resonance of Electrons and of Holes in Cuprous Oxide, Cu_2O. *J. Phys. C: Solid State Phys.* **1976**, *9*, 1429−1439.